# Singlet Fission via an Excimer-Like Intermediate in 3,6-Bis(thiophen-2-yl)diketopyrrolopyrrole Derivatives

Catherine M. Mauck, Patrick E. Hartnett, Eric A. Margulies, Lin Ma, Claire E. Miller, George C. Schatz,* Tobin J. Marks,* and Michael R. Wasielewski*

Department of Chemistry, Argonne-Northwestern Solar Energy Research (ANSER) Center, and Institute for Sustainability and Energy at Northwestern, Northwestern University, Evanston, Illinois 60208-3113, United States

S *Supporting Information*

ABSTRACT: Singlet fission (SF) in polycrystalline thin films of four 3,6-bis(thiophen-2-yl)diketopyrrolopyrrole (TDPP) chromophores with methyl (**Me**), *n*-hexyl (**C6**), triethylene glycol (**TEG**), and 2-ethylhexyl (**EH**) substituents at the 2,5-positions is found to involve an intermediate excimer-like state. The four different substituents yield four distinct intermolecular packing geometries, resulting in variable intermolecular charge transfer (CT) interactions in the solid. SF from the excimer state of **Me**, **C6**, **TEG**, and **EH** takes place in τ_{SF} = 22, 336, 195, and 1200 ps, respectively, to give triplet yields of 200%, 110%, 110%, and 70%, respectively. The transient spectra of the excimer-like state and its energetic proximity to the lowest excited singlet state in these derivatives suggests that this state may be the multiexciton $^1(T_1T_1)$ state that precedes formation of the uncorrelated triplet excitons. The excimer decay rates correlate well with the SF efficiencies and the degree of intermolecular donor–acceptor interactions resulting from π-stacking of the thiophene donor of one molecule with the DPP core acceptor in another molecule as observed in the crystal structures. Such interactions are found to also increase with the SF coupling energies, as calculated for each derivative. These structural and spectroscopic studies afford a better understanding of the electronic interactions that enhance SF in chromophores having strong intra- and intermolecular CT character.
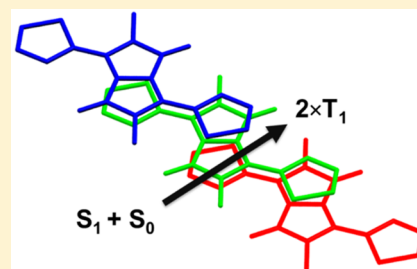
■ INTRODUCTION

Singlet exciton fission (SF) is the photophysical process in which absorption of a photon by an assembly of two or more organic chromophores produces a singlet exciton that subsequently results in spin-allowed formation of two triplet excitons. While this process has been known for more than 50 years,[1] it has recently received broad renewed attention because it promises a way to increase the overall efficiency of solar photovoltaics from the 32% Shockley-Queisser limit to nearly 45% in ideal systems.[2] Apart from efforts to identify new photochemically robust chromophores that undergo SF to produce triplet states with the maximal 200% efficiency, recent work in this field has focused on understanding how the detailed electronic couplings between adjacent SF chromophores dictated by their relative geometry determine the efficiency of this process and which intermediate electronic states are involved in the SF mechanism. Studies have been directed toward understanding SF in pentacene,[3−7] tetracene,[8,9] and other SF chromophores such as diphenylisobenzofuran,[10,11] carotenoids,[12,13] and polythiophenes.[14,15] In addition, work on the more stable TIPS-substituted pentacene[3,4,16,17] and rylene-based chromophores[18,19] has recently yielded promising results. The high efficiency and ultrafast SF rate of pentacene has already inspired SF-based photovoltaics that display external quantum efficiencies >100%, establishing the significance of SF for photovoltaics development.[20−22] Many recent theoretical and mechanistic SF studies have focused on

polyacenes; however, the general applicability of the insights gleaned from these studies to other chromophores has received less attention.

SF can occur by two general mechanisms: one that directly couples the initial $^1(S_1S_0)$ state to a multiexciton $^1(T_1T_1)$ state by a two-electron process and another that proceeds through a charge transfer (CT) state by two consecutive one-electron processes.[1] However, the interactions of the various states involved in SF have recently been shown to be far more complex; in particular the nature of the $^1(S_1S_0)$ and $^1(T_1T_1)$ states and their interactions.[5,6,23−26] For example, several studies of polyacenes have proposed that an excimer or excimer-like state is also involved in SF,[3,5,27,28] with some studies identifying this excimer as a hybrid state having both singlet and triplet character, as well as identifying the excimer-like state with the $^1(T_1T_1)$ multiexciton state. In addition, work on polyacenes as well as donor−acceptor oligomers has highlighted the potential importance of CT states, which may be the excimer state with significant CT character.[26,29] In order to probe the generality of these mechanistic ideas, it is important to explore comparable phenomena in several types of SF chromophores.

Diketopyrrolopyrroles (DPPs) comprise a large class of dyes known for their strong visible absorption ($\varepsilon > 10^4$ M^{-1} cm^{-1})
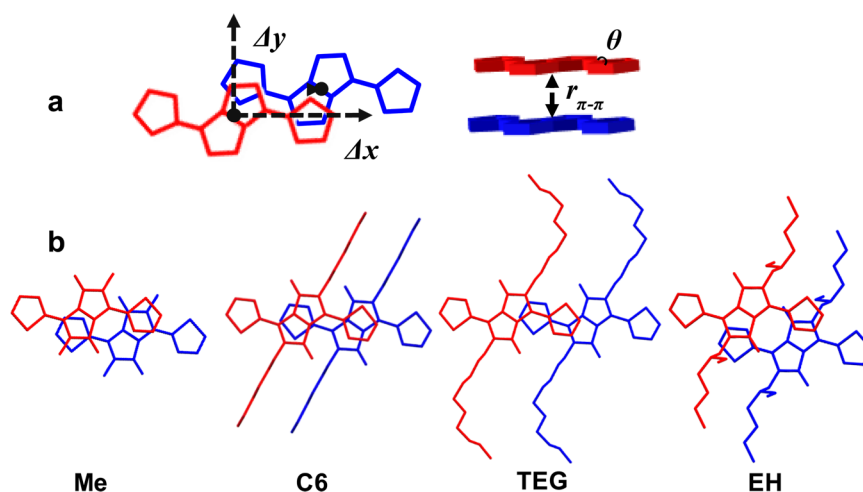
Figure 1. Structural characterization of intermolecular geometry in TDPPs. (a) Diagram of transverse (Δx) and longitudinal (Δy) offset axes measured from the center point of the DPP core, and the $\pi-\pi$ distance ($r_{\pi-\pi}$) between the two planes of DPP cores in the TDPP dimer unit. (b) Dimer unit representing the intermolecular geometry for **Me**, **C6**, **TEG**, and **EH**. Dimer units were extracted from experimental or published crystal structure data as noted in main text.

with substantial chemical and photostability.[30] DPPs are synthetically tunable, highly fluorescent, and typically possess high charge carrier mobilities in the solid state. These properties have stimulated extensive investigation of DPP-based small molecules and conjugated polymers as semiconductors in organic photovoltaics (OPVs) and field effect transistors (OFETs).[30−37] DPP dyes are based on the bicyclic 2,5-dihydropyrrolo[4,3-c]pyrrolo-1,4-dione core, flanked at the 3,6 positions by aryl groups such as 3,6-diphenyl (PhDPP) or 3,6-bis(thiophen-2-yl) (TDPP) as seen in Figure 1. Alkyl substitution at their 2,5 ring nitrogen positions renders these compounds highly soluble in common organic solvents, while modification of the aryl groups allows for tuning of electronic properties.[38−41] Side chain substitution has only minor effects on the electronic properties of DPP in solution but strongly influences solid state packing, fluorescence, and charge transport. These properties have been the subject of extensive studies, particularly in the case of TDPP,[39,41−46] which is the most commonly investigated DPP in organic electronics, due to its low cost, high carrier mobility,[37] and synthetic flexibility.[47,48]

The singlet excited state energy of TDPP is 2.2 eV, and the corresponding triplet excited state energy is 1.1 eV;[32,49] thus, these energies fulfill the relationship $E(S_1) \geq 2E(T_1)$ for exoergic SF.[1] We recently observed efficient SF for the first time in a variety of 3,6-diaryl-substituted DPP derivatives, where the aryl substituents are phenyl (Ph), 5-phenylthiophen-2-yl (PhT), and thiophen-2-yl (T).[50] In the PhT derivative, the triplet yield was found to be ≥165% with SF taking place in 220 ± 20 ps. These three molecules display a range of $\pi-\pi$ stacking distances in polycrystalline thin films, which is hypothesized to govern SF because intermolecular coupling is known to have a large effect on SF efficiency.[1]

Recent theoretical modeling has focused on mapping the transverse and longitudinal offsets at given π-stacking distances to discern how these parameters influence SF,[51,52] and several experimental studies have compared SF efficiencies for the different molecular packing geometries of diphenylisobenzofuran, polyacenes, and rylene derivatives.[10,11,18,51,53−56] The effect of intermolecular geometry on SF efficiency in these previous studies motivates the present work, since solid-state packing in TDPPs is easily varied by 2,5-dialkyl side chain modification.

DPPs readily crystallize due to strong $\pi-\pi$ interactions[35,38] including intermolecular donor−acceptor (D-A) interactions between the thiophene ring of one molecule and the DPP core of an adjacent molecule.[57] These interactions are particularly strong in TDPPs due to the coplanarity of the thiophenes and the DPP core.[36] We now report on four TDPP derivatives having systematically varied 2,5-alkyl substitution: methyl (**Me**), n-hexyl (**C6**), triethylene glycol (**TEG**), and 2-ethylhexyl (**EH**) (Scheme 1). It will be seen that this model system offers

Scheme 1. Synthesis and Nomenclature for the TDPP Series Investigated Here
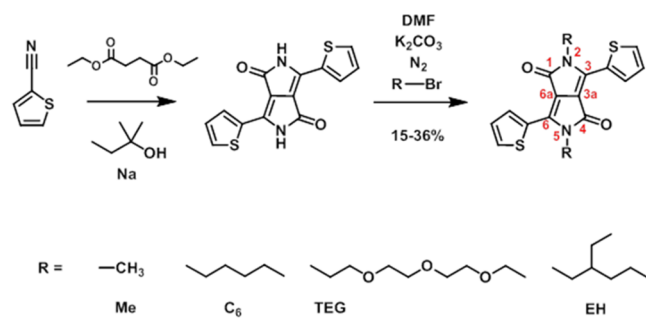
a way to fine-tune the degree of slip-stacking, with only a small variation in the $\pi-\pi$ distance across the four derivatives, which, in turn, results in a variable CT interaction between the stacked TDPPs. Importantly, these changes in slip-stacking result in differing amounts of an intermediate excimer-like state being observed that is directly connected to triplet formation by SF. In addition, through this tuning, we find that the SF rate can be enhanced by an order of magnitude in TDPP compared to our previous results, making SF in DPP more viable for potential SF charge generation. The ability to achieve such geometries without significantly changing the SF energetics and $\pi-\pi$ stacking distance is important for understanding the mechanistic role that intermolecular coupling plays in SF and will inform the design of next-generation DPP-based chromophores with high stability and even more rapid SF rates.

■ EXPERIMENTAL SECTION

Materials Synthesis. TDPP derivatives **Me**, **C6**, **TEG**, and **EH** were synthesized following literature procedures as shown in Scheme 1.[48] Palladium octabutoxyphthalocyanine (PdPc(OBu)$_8$) was also synthesized following published methods.[58] TDPP derivatives were purified via gradient sublimation (3 × 10^{-6} Torr) prior to vapor deposition on glass substrates.

Crystallography. A single crystal of **Me** was grown by slow diffusion of methanol vapor into a chloroform solution, and mounted on a MiTeGen MicroLoop with Paratone oil under an N$_2$ stream (100 K) in a Bruker AXS APEX2 diffractometer equipped with a charge-coupled device (CCD) detector and a Cu Kα microfocus source, with Quazar optics. The data were corrected for absorption (SADABS) and structure determination was performed using SHELXS and refined using SHELXL. All non-hydrogen atoms were refined nonisotropically.

Sample Preparation. Thin film samples were deposited on glass substrates (RT) at a rate of 0.5 Å/s in a vacuum thermal evaporator (Denton Vacuum DV502-A). Vapor deposition was monitored with an in situ quartz crystal microbalance. Samples were stored under N$_2$ or in an evacuated environment prior to measurements. Films were annealed under dichloromethane vapor at room temperature in a glass Petri dish for 1.0 h. Film thicknesses were measured with a Veeco Dektak 150 surface profilometer with a 6.5 μm diameter stylus.

Grazing Incidence X-ray Scattering (GIWAXS). Measurements were performed on thin film samples at the dedicated high-resolution grazing-incidence X-ray scattering beamline 8-ID-E at the Advanced Photon Source at Argonne National Laboratory. A 7.35 keV, 1.6868 Å X-ray beam at an incident angle of 0.2° was directed at the sample, maximizing scattering from the film while minimizing glass substrate scattering. Scattered light was collected with a Pilatus 1 M detector 204 mm from the sample. Coordinates in the GIWAXS spectra are expressed as a function of $q = 2\pi/d$ where $d = \sin(\theta)/\lambda$. The detector images were then processed using GIXSGUI to apply pixel efficiency, polarization, flat field and solid angle corrections.[59] Further data analysis was performed to fit the GIWAXS images to crystal structure parameters using the Diffraction Pattern Calculator (DPC) Toolkit.[60]

Steady State Spectroscopy. A Shimadzu UV-1800 spectrometer was used to measure the steady state optical absorption spectra of solution samples. Steady state photoluminescence spectra were measured using a HORIBA Nanolog fluorimeter. Scatter-corrected absorption spectra for film samples were acquired on a PerkinElmer LAMBDA 1050 UV/vis/NIR spectrometer in an integrating sphere (150 mm). Scatter-corrected absorption spectra were calculated using the sum of reflected and transmitted light and the Beer–Lambert law.

Femtosecond Transient Absorption Spectroscopy (fsTA). The experimental setup has been previously described.[18] In brief, the 1040 nm fundamental output of a 100 kHz amplifier (4.5 W, 350 fs, Spirit 1040-4, Spectra Physics) is split by a beam splitter. The smaller fraction (0.50 W) is focused to a ∼ 40 um spot size in a 5 mm undoped yttrium aluminum garnet (YAG) crystal to generate a white light continuum probe pulse (480–1100 nm). The larger fraction (4.0 W) drives a noncollinear optical parametric amplifier (Spirit-NOPA-3H, Spectra Physics) to generate 75 fs, 500–800 nm pump pulses. The pump and probe polarizations are set at the magic angle relative to one another. After passing through the sample, the continuum probe beam is spectrally dispersed in a modified SPEX 270m monochromator on a 600 groove/mm grating, once passed through the sample. The dispersed probe beam is then directed onto a CMOS linear image sensor (S10112-512Q, Hamamatsu) by a 2 in diameter Ag mirror. The pump beam is chopped prior to the sample at 476 Hz for signal differencing. The instrument response function is approximately 100–150 fs and the average total exposure time per data point is 5 s, resulting in 5 × 10^{-6} OD baseline noise. During fsTA experiments, film samples were placed under vacuum in a cryostat (VPF-100, Janis Research, 1 × 10^{-2} Torr) to minimize photodegradation, and irradiated with 515 nm, 15–30 nJ pump pulses through a 1.000 mm diameter pinhole positioned directly in front of the sample in the cryostat chamber (2.8–3.8 μJ/cm^2). By focusing the pump beam with a long focal length lens, the spot size at the sample is equal to the pinhole diameter.

Nanosecond Transient Absorption Spectroscopy (nsTA). The frequency-tripled output of a Continuum Precision II 8000 Nd:YAG laser was used to pump a Continuum Panther OPO to generate a pump excitation beam with a 7 ns, 515 nm pulse at 1.41 mJ. A xenon flashlamp (EG&G Electro-Optics FX-249) generated the probe pulse, which was then overlapped on the sample with the pump spot size focused to slightly larger than the probe through a 1.0 cm diameter aperture. Films were measured under vacuum in a VPF-100 (Janis Research) cryostat as described above. Kinetic traces were recorded with an oscilloscope (LeCroy Wavesurfer 42Xs) interfaced with a customized LabVIEW program (LabVIEW v. 8.6.1), and acquired using a monochromator and Hamamatsu R928 photo-multiplier tube, acquired in 5 nm intervals from 430−800 nm; and in 1 nm intervals from 560 to 600 nm for **Me**, 580−630 nm for **C6**, 545−585 nm for **TEG**, and 550−600 nm for **EH**. Spectra were constructed by merging the kinetic traces (averaged over 10−20 ns, 150 shots per kinetic trace).

Time-Resolved Fluorescence Spectroscopy (TRF). The same high repetition rate (100 kHz) ultrafast laser system described above for the fsTA setup was used as the laser source in time-resolved fluorescence measurements. The 515 nm, 75 fs, 1 nJ laser pulses from a Spirit-NOPA-3H were utilized as the excitation source. Picosecond time-resolved fluorescence data were collected at room temperature using a streak camera system (Hamamatsu C4334 Streakscope), for which the instrument response function (IRF) is 20 ps.

Film Sensitization Experiments. To determine the spectral signature of the triplet state for each TDPP derivative, doped films were prepared using a triplet sensitizer, similar to previous methods in the literature.[27,50,61−63] Films were spin-coated from a 20:1 w/w PdPc(OBu)$_8$:TDPP or polystyrene solution. First, a 1 mg/mL solution of PdPc(OBu)$_8$ in chloroform was used to prepare 20 mg/mL solutions of each TDPP derivative and of polystyrene. Films were spin-coated from these solutions at 1000 rpm on glass coverslips. Sensitized films were not annealed in order to avoid phase segregation between the sensitizer and sensitized compounds. Sensitized films were then excited with a 730 nm pump beam using the fsTA system described above. By exciting PdPc(OBu)$_8$ to its S$_1$ state (1.71 eV), followed by rapid intersystem crossing (τ_{ISC} = 11 ps) to the PdPc(OBu)$_8$ T$_1$ state (1.24 eV),[58,62] the TDPP triplet state (∼1.1 eV) is populated via triplet−triplet energy transfer. Sensitized triplet difference spectra were obtained by subtracting residual PdPc(OBu)$_8$ triplet signal from the sensitized TDPP film spectra (Figure S7).

Kinetic Analyses. Global analysis of the fsTA data was performed by simultaneous fitting of ΔA(t) at selected wavelengths for each sample to the analytic solution to the coupled differential equations for a specified kinetic model,[64] convoluted with the Gaussian instrument response function. This process, using a custom MATLAB program, has been previously described in further detail.[65] The species-associated kinetic model used to fit the data is represented by eq 1, in which state A (taken to be S$_1$) decays to an intermediate state B, prior to forming state C (T$_1$).

$$\frac{d[A]}{dt} = -k_1[A]; \; \frac{d[B]}{dt} = k_1[A] - k_2[B]; \; \frac{d[C]}{dt} = k_2[B] - k_3[C] \tag{1}$$

The resulting global fit of wavelengths gives k_1 and k_2, which correspond to A → B and B → C, respectively, as well as k_3, which for all data sets was greater than the delay window (8 ns). Species-associated spectra are extracted from this analysis, which correspond to the states specified in the model. Although various models were tried, such as a simpler two-state model and one incorporating annihilation events, the best fit was achieved for all data sets with eq 1.

The psTRF intensity vs time and wavelength data sets of the annealed films were also fit to the kinetic model described in eq 1. However, for this global analysis, singular value decomposition (SVD) was performed in the custom MATLAB program. Deconvolution of the two-dimensional spectra produced an orthonormal set of basis

spectra describing the species' wavelength dependence and their corresponding orthogonal vectors describing the time-dependent amplitudes of the basis spectra.[66] A linear combination of the amplitude vectors were fit to the species-associated kinetic model,[64] and the species spectra were then constructed from the same linear combination of the basis spectra.

RESULTS

Structural Characterization. The crystal structures for **C6**, **TEG**, and **EH** have been previously reported.[41] We report here the crystal structure for **Me**, which crystallizes in the monoclinic crystal system in the $P2_1/c$ space group with a total of two molecules in the unit cell and parameters of $a = 11.2356$ Å, $b = 12.9918$ Å, $c = 11.3681$ Å, $\beta = 154.939°$. The compound packs in a π-stacked geometry arranged in a herringbone pattern between stacks, similar to the other TDPP derivatives. Further crystallographic details are given in the Supporting Information.

By extracting the most closely associated dimer units from each crystal structure, intermolecular interactions can be characterized as shown in Figure 1, as a function of the distance between the core planes $r_{\pi-\pi}$, and longitudinal (Δy) or transverse (Δx) displacement, measured from the DPP core center point. Due to the presence of the five-membered thiophene ring,[35] all four TDPP molecules display a high degree of planarity, with torsional angles between the thiophene and DPP core ranging from $\theta = 19.1°$ and $11.0°$ for **EH** and **C6** to $\theta = 2.7°$ and $4.1°$ for **Me** and **TEG**, respectively. We adopt molecular axis notation as in previous DPP literature,[39] in which Δy is measured along the short axis and Δx along the long axis, which is also approximately the axis of the $S_1 \leftarrow S_0$ transition dipole moment.[44] These parameters in large part determine the electronic couplings that govern SF.[1,51,67]

Diffraction-derived values for $r_{\pi-\pi}$ are compiled in Table 1. Measured distances are all within 3.3–3.7 Å, indicating that the

Table 1. Structural Information for Dimer Pairs Extracted from Crystallographic Data, Including Torsion Angle θ between Thiophene Ring and DPP Core; Intermolecular $\pi-\pi$ Stacking Distance $r_{\pi-\pi}$; and Transverse (Δx) and Longitudinal (Δy) Displacement

TDPP	θ (deg)	$r_{\pi-\pi}$ (Å)	Δx (Å)	Δy (Å)
Me	2.7	3.27	3.32	1.53
C6	11.1	3.50	4.13	0.13
TEG	4.1	3.70	6.26	0.04
EH	19.1	3.55	3.60	2.25

TDPPs studied here are in the strongly coupled regime. **Me** displays the shortest $\pi-\pi$ distance of 3.27 Å, whereas **TEG** has the longest at 3.70 Å. The other two derivatives **C6** and **EH** have very similar distances of 3.50 and 3.55 Å respectively. The longitudinal (Δy) and transverse (Δx) offsets are also given in Table 1. Along the transverse axis, all molecules are slipped by at least 3.3 Å in the dimer pair, a distance that roughly corresponds to the length of one thiophene ring bonded to the DPP core ($\sim$3.9 Å) and allows the thiophene ring to occupy a position above the DPP core of an adjacent molecule, as seen in **Me**, **C6**, and **EH** which have Δx values of 3.32, 4.13, and 3.60 Å, respectively.

The displacement along the longitudinal axis then modulates the strength of the $\pi-\pi$ interaction; for example, **EH** has a transverse offset that places the ring above the core but has the

largest value of Δy at 2.25 Å, which leads to the least overlap between the donor and acceptor units. In contrast, **C6** is barely offset in the longitudinal direction (0.13 Å), and the D–A interaction is prominent. Similarly, although its longitudinal offset is more significant (1.53 Å), **Me** also displays a strong ring/core overlap in the dimer pair. With the smallest $r_{\pi-\pi}$ value, this interaction is presumably more greatly enhanced in **Me**. **TEG** differs with respect to the other three derivatives in that its transverse offset is large: the thiophene ring is now positioned between the ring and core below, slipped by 6.26 Å. With negligible offset in the longitudinal direction (0.04 Å), this structure represents an intermediate arrangement, in which the D–A interaction is still present, but less pronounced than in **Me** and **C6**.

Film Characterization. As-deposited and annealed thin films were characterized by grazing incidence wide-angle X-ray scattering (GIWAXS), and the resulting scattering patterns are shown in Figures S1 and S2. GIWAXS yields information about thin film structural changes upon thermal annealing and how the vapor-deposited thin films compare to the reported crystal structure of each molecule. All thin films studied were polycrystalline, and Scherrer analysis[68] demonstrates in all cases that annealing increases the crystallinity (Table S1–S2). The crystallite dimensions calculated from this analysis (D_{hkl}) are far larger than typical exciton diffusion lengths,[69] and because of this length scale relationship, it is reasonable to assume that the excitons seldom reach an interface and that the observed photophysics originates from within the crystallites.

Using a MATLAB fitting script input with the crystal structure parameters,[59] unit cell values were calculated from the GIWAXS spectra for **C6**, **TEG**, and **EH** to determine if and how the microstructures of the as-deposited and annealed thin films deviate from those of the single crystals (Table S1). Note that **Me** crystallites do not show as strong a preferred orientation in the films and as such cannot be fit using the MATLAB script. Instead, the in-plane and out-of-plane patterns are compared to the calculated powder pattern and their linecuts are compared to find a slight preferred orientation (Figure S2). The unannealed film of **Me** has an additional peak at 9.7° compared to the calculated powder pattern, which disappears upon solvent vapor annealing. This peak most likely results from a polymorph that is then converted to the single crystal structure upon annealing.

For films of **C6**, **TEG**, and **EH**, the fit GIWAXS spectra closely match the reported single crystal structures for both the as-deposited and annealed films. **C6** and **EH** deviate <1% from the crystal structure parameters. **TEG** displays slightly shortened b and c unit cell axes in the thin film (<5% compared versus the single crystal structure). **TEG** also exhibits the greatest change upon annealing, perhaps due to the effects of the conformationally flexible triethylene glycol side chains which are more likely to cause disorder. With the exception of the peak at 9.7°, which disappears upon annealing, films of **Me** also correspond closely to the expected diffraction pattern. Given these results, an interpretation of intermolecular geometries in the film based on single crystal parameters is physically reasonable.

Optical Characterization in Solution. Steady-state optical absorption and fluorescence spectra of the four TDPPs in toluene are shown in Figure 2. The solution steady-state absorption spectra are similar, with peaks at 552 and 513 nm for molecules **Me**, **C6**, and **EH**, and at 546 and 509 nm for **TEG**. This strong visible absorption band has been
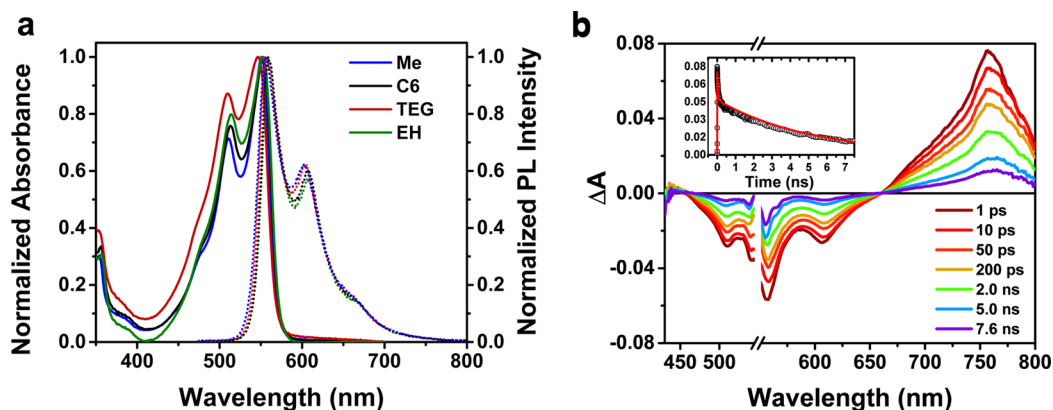
Figure 2. (a) Solution steady-state absorption (solid line) and fluorescence (dashed line) spectra. (b) Solution fsTA spectra for **C6** in dichloromethane (OD 0.2), excited at 550 nm. Inset: The corresponding kinetics for ESA decay of **C6** at 770 nm (black circles) and fit to the data (red solid line). The data are representative of all four TDPP derivatives.
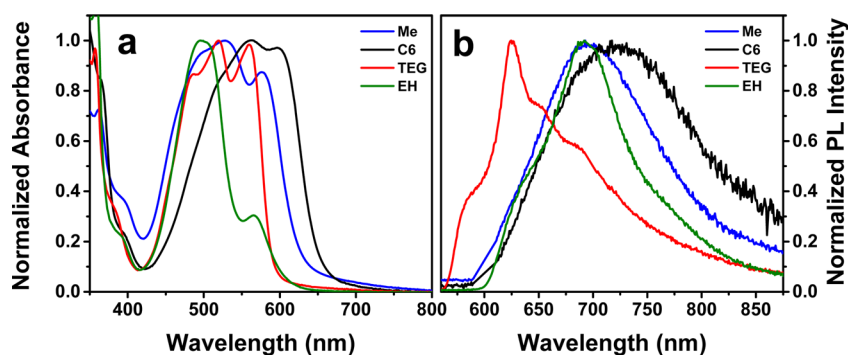

Figure 3. Normalized steady-state optical absorption (a) and fluorescence (b) spectra of TDPP chromophores after solvent-vapor annealing for 1 h in dichloromethane.

assigned to a HOMO → LUMO $\pi \to \pi^*$ intramolecular charge transfer (ICT) transition in similar DPP systems.[41] An additional absorption around 350 nm is also observed, and all four compounds are highly fluorescent in agreement with previously characterized DPPs.[40,41,49,70] The fluorescence maximum of derivatives **EH** and **C6** is at 560 nm, while that of **Me** and **TEG** is slightly blue-shifted to 556 nm. The optical bandgaps were measured at the crossing point of the absorption and fluorescence spectra to be 2.23−2.24 eV for all four derivatives.

All TDPPs were also studied in solution (CH_2Cl_2, OD ∼ 0.2) using transient absorption spectroscopy (Figure 2b). Following 550 nm excitation, ground state bleach (GSB) and stimulated emission (SE) are seen as a negative signal between 450−650 nm with a positive excited state absorption (ESA) having a 755 nm maximum. The decay of the ESA for all four derivatives was fit to a biexponential decay with $\tau_1 \sim 50$ ps (30%) and $\tau_2 = 5.2 \pm 0.1$ ns (70%) in agreement with kinetics reported in the literature.[32,71] The shorter time constant is assigned to a structural relaxation in the S_1 (ICT) state most likely due to planarization of the thiophene donor relative to the DPP core acceptor. This behavior is not observed in the polycrystalline solid films (see below) because the thiophene donor and DPP core are already fixed in a nearly coplanar geometry in the solid. Note that there is no long-lived triplet state signal observed for monomeric TDPP in solution, because the intrinsic intersystem crossing yield is <1%,[70,72,73] with a 74% quantum yield of fluorescence.[40]

Steady-state Optical Characterization of the Annealed Films. Figure 3 shows the optical absorption spectra of the annealed TDPP films. Intermolecular electronic interactions produce significant shifts in the visible region spectra, indicating strong coupling between the chromophores. All derivatives display absorption shifts toward longer wavelengths in the solid state, in agreement with previous modeling of TDPP solid-state spectra with two Davydov components, and packing which enhances intermolecular donor−acceptor interactions.[44] The absorption spectrum of **EH** is dominated by a blue-shifted band at 500 nm, whereas in **Me**, **C6**, and **TEG** the dominant bands occur at lower energies than in their solution spectra. Molecules **Me** and **C6** evidence the greatest spectral changes, with large bathochromic shifts and broadening in the solid state. The absorption of the **TEG** thin film is somewhat intermediate between the most strongly coupled (**Me**) and branched (**EH**) TDPPs; the film spectrum of **TEG** resembles the solution spectrum more closely with two sharp peaks, although the absorption band maximum is also red-shifted to 560 nm.

Although the **Me** derivative has the shortest TDPP $\pi−\pi$ stacking distance (3.27 Å), which should lead to stronger electronic coupling, **C6** has a $\pi−\pi$ stacking distance (3.50 Å) quite close to that of branched **EH** (3.55 Å), indicating that the $\pi−\pi$ stacking distance alone does not explain the observed shift. In the crystal structures of **Me** and **C6**, the electron-rich thiophene ring is positioned directly over the electron-deficient DPP core, plausibly leading to a strong D−A interaction. In other TDPP systems this phenomenon has been suggested to
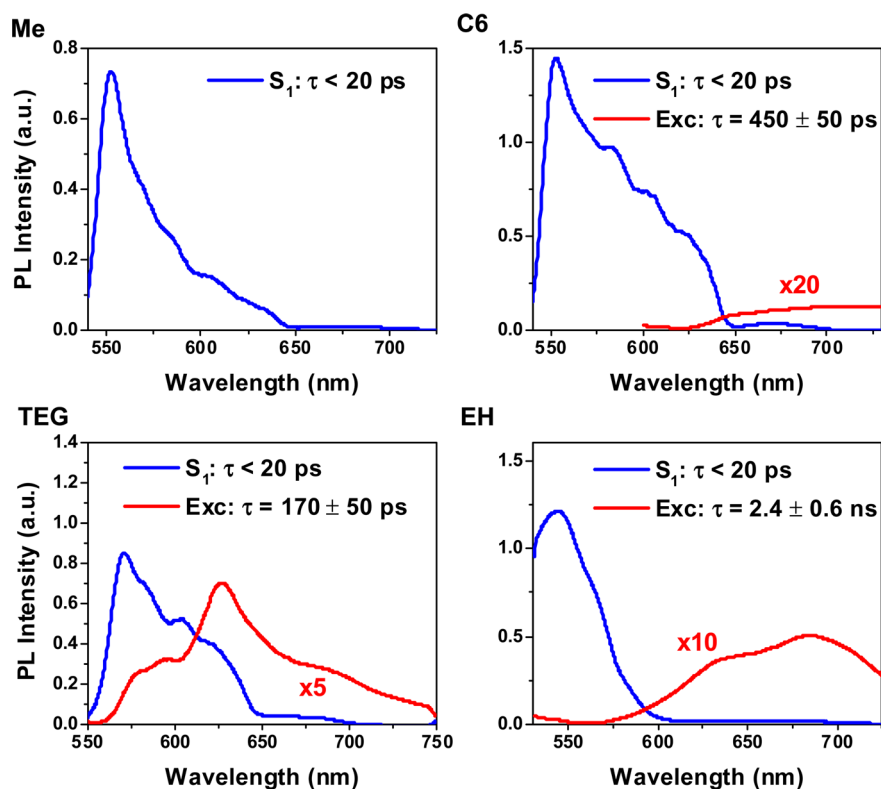
Figure 4. Species-associated psTRF fluorescence spectra for the indicated annealed TDPP films following 515 nm excitation at 515 nm. The spectra were fit to the model specified by eq 1 in which S_1 decays in τ_{S_1} and Exc decays in τ_{Exc}.

contract the intermolecular distance and increase the coupling with a stabilizing admixture of CT character.[44]

Figure S3 shows the as-deposited TDPP film absorption spectra. In the case of the highly crystalline films of **C6**, **TEG**, and **EH**, solvent vapor annealing has very little effect on the steady-state structural and optical properties. However, in the case of **Me**, annealing results in a more significant optical change. The origin of this effect may be the polymorph that is converted to the dominant structure, as evidenced by the disappearance upon annealing of the 2θ peak at 9.7° in the GIXRD pattern (Figure S2). However, the photophysical data for as-deposited films are overall quite similar to those of the annealed films and are provided in the Supporting Information for comparison (Figure S6).

In contrast to the solution fluorescence spectra (Figure 2a), the steady-state photoluminescence spectra of the films are broad, red-shifted, and featureless (Figure 3b), qualities which often indicate the presence of excimers. Moreover, the fluorescence quantum yields of the annealed films are all <1%. Although the peak maxima for **Me**, **C6**, and **EH** emission are all quite similar (1.7–1.8 eV) with onset at ~2.1 eV, **TEG** is notable for the distinct vibronic structure in its fluorescence spectrum with a maximum at 625 nm (2.0 eV) in addition to the redder excimer-like emission.

Time-Resolved Fluorescence Spectroscopy of the Annealed TDPP Films. Annealed films were characterized by picosecond time-resolved fluorescence (psTRF) spectroscopy using 515 nm excitation and analyzed by SVD using the first-order three-state model given in eq 1. The resulting species-associated spectra are shown in Figure 4, with raw spectra in Figure S4. In all molecules, the initial, strong emissive signal resembles the monomeric fluorescence in Figure 2a, having maxima between 540–570 nm with vibronic structure

extending to 650 nm. This state decays rapidly, within the instrument response function (IRF, ~20 ps), to a broad, featureless emission observed between 600–725 nm in both **C6** and **EH**, which appears within the IRF and decays with lifetimes of $\tau = 450 \pm 50$ ps and $\tau = 2.4 \pm 0.6$ ns for **C6** and **EH**, respectively. This broad emission band in **C6** is much weaker than the S_1 fluorescence (>100:1), in contrast to **EH**, where this emission band is somewhat more intense (20:1). The resulting global fits for each derivative yield the emission spectra and kinetics shown in Figure 4. No such red-shifted emission is observed for **Me**. However, the TRF signal for **TEG** is dominated by S_1 fluorescence at early times, followed by emission from the red-shifted excimer-like species emitting at 625 nm. The resulting global fit gave $\tau_2 = 170 \pm 50$ ps. The large error bars on the fluorescence lifetimes result from the fact that the emission spectra are very weak. No other emission was detected within the 1 ns delay window.

Femtosecond Transient Absorption Spectroscopy of Annealed TDPP Films. Film samples were excited at 515 nm with sufficiently low pump energies (15–30 nJ/pulse) to minimize singlet–singlet exciton annihilation,[74] with excitation densities on the order of 10^{17} cm^3. Calculated excitation densities for each derivative are given in the Supporting Information (Table S5), as well as a power dependence study which shows that the kinetics are constant within this range of pulse energies. At these low fluences, photoinduced heating effects are expected to be minimal, using the method of Rao et al. to calculate an upper limit of heating from photoexcitation,[75] assuming heat capacities similar to those measured for a PhDPP crystal.[76] We calculate that, for example, in **Me** the upper limit would be ≤0.08 K, with 515 nm, 30 nJ pump pulses with a 1 mm spot size and a film thickness of 196 nm.
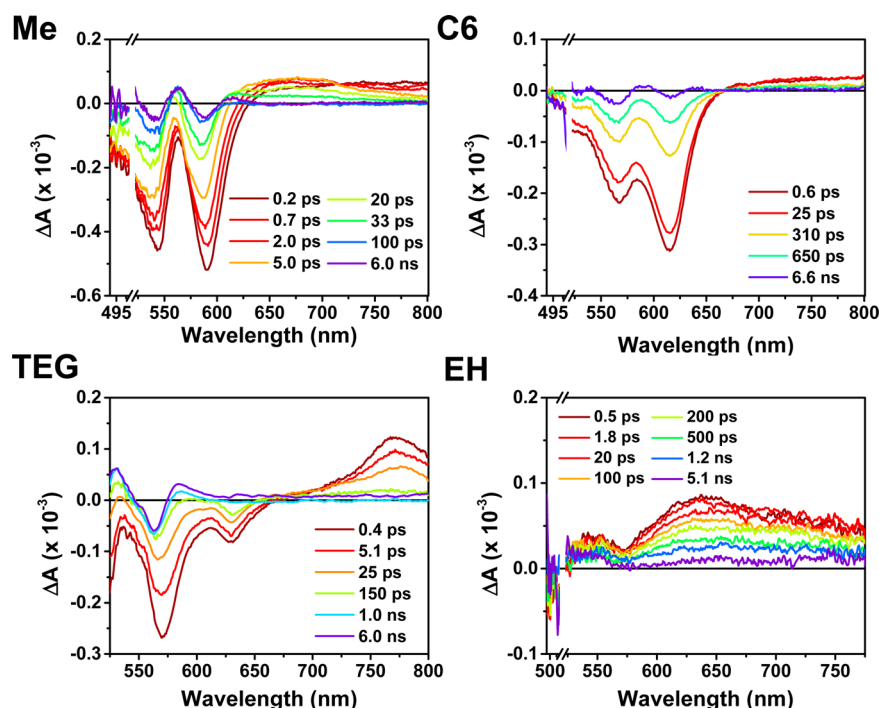
Figure 5. Femtosecond transient absorption spectra for annealed films with a 3.8 μJ/cm² pump pulse at 515 nm.
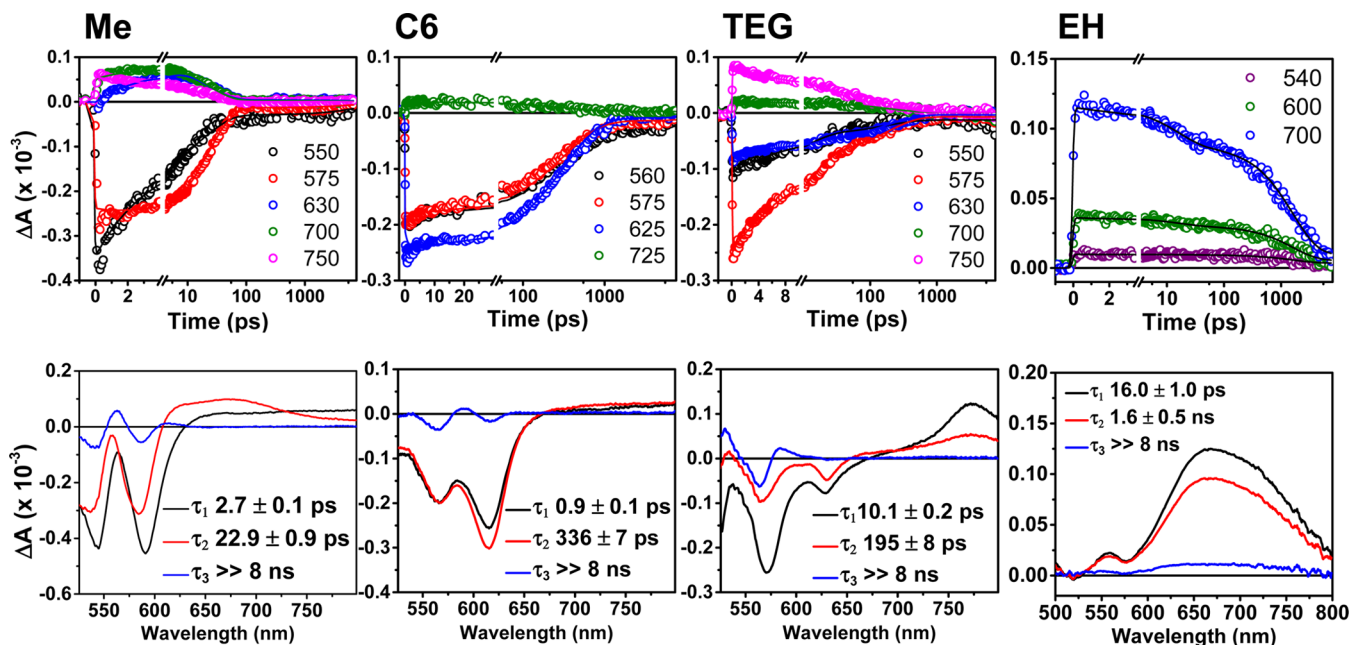

Figure 6. Globally fit wavelength kinetics (top) and species-associated spectra (bottom), fit globally over multiple selected wavelengths of the fsTA data for TDPP films. Each data set was fit to the A → B → C model described by eq 1.

The spectra of the annealed films from 0 to 8 ns are shown in Figure 5, while data from the as-deposited films are given in Figure S6. The data for the annealed films were best fit to the three-state kinetic model given by eq 1 (see Experimental). The kinetics at selected wavelengths from the global analysis are shown in Figure 6, in addition to the resulting species-associated spectra for states A, B, and C. The time constants that result from the global fits, $\tau_1 = 1/k_1$ and $\tau_2 = 1/k_2$ are given in Table 2.

For **Me**, the broad ESA from 620−800 nm shifts within τ = 2.7 ± 0.1 ps to the intermediate spectrum in the red trace,

which forms state C in τ = 22.1 ± 0.9 ps that is nearly identical to the alternating, wave-like signal previously reported for the triplet difference spectra for PhDPPs and TDPPs (see next section).[50,72,73] For states A and B, the GSB signals overlap, but in going from A → B a blue-shift occurs for the two GSB features at 545 and 595 nm, which likely corresponds to the loss of the stimulated emission. **C6** has a very weak, broad ESA from 660−800 nm for species A and B; the globally fit spectra for these two states are very similar, but a clear shift or increase in the intensity occurs between 660−725 nm going from A to B. The triplet state is formed from intermediate state B in τ_2 =

Table 2. Globally Fit Kinetic Rate Constants (τ_1 and τ_2) and Triplet Yields Φ_T for TDPP Films[a]

TDPP	τ_1 (ps)	τ_2 (ps)	Φ_T
Me	2.7 ± 0.1	22.1 ± 0.9	2.0 ± 0.2
C6	0.9 ± 0.1	336 ± 7	1.1 ± 0.2
TEG	10.1 ± 0.2	195 ± 8	1.1 ± 0.2
EH	16.0 ± 1.0	1600 ± 500	0.7 ± 0.2

[a]Each dataset was fit to an A → B → C model in which A = S_1, B = excimer-like intermediate, and C = T_1. Lifetime τ_1 corresponds to the formation of the intermediate state. Lifetime τ_2 corresponds to triplet formation.

336 ± 7 ps. The kinetics agree with the fluorescence kinetics, in which the highly emissive state is quenched in <20 ps and the weakly emissive species decays over a longer time.

TEG has an ESA maximum around 775 nm, similar to the solution fsTA spectra in Figure 2, with the stimulated emission peaks decaying at the same time as the ESA to state B in τ = 10.1 ± 0.2 ps. This intermediate, broad ESA is slightly blue-shifted as can be seen between 650−700 nm, similar to what is observed for **Me** and **C6**. State B decays to the **TEG** triplet in τ = 195 ± 8 ps. Finally, the spectrum for **EH** displays a broad ESA from 525−800 nm, with the GSB appearing on top of this positive signal, from 500−600 nm. Because the ground state absorption is blue-shifted outside of the detection window, there is little spectral difference between the three states; however, intermediate state B shows a small amount of increased broadening in particular between 600−500. By globally fitting the wavelengths shown in Figure 6, we find that τ_1 = 16.0 ± 1.0 ps and τ_2 = 1.6 ± 0.5 ns. The blue trace that should represent the triplet state clearly still has residual excimer-like ESA, as the lifetime of this intermediate state is measured by psTRF to be τ = 2.4 ns. The rate constant for triplet formation (k_2) in the proposed kinetic model may be difficult to interpret from this global analysis because it is on the order of the time scale of the experiment (8 ns), and the species associated spectra show few distinguishing characteristics.

From the spectral global analyses, an intermediate state kinetic model afforded the best fit to all data sets, despite attempts to fit the data to a direct mechanism (S_1 to T_1) and a model in which excimer decay was a parallel process to triplet formation. This was especially true for **Me** and **TEG**. However, we note that a less clean fit could be achieved for **C6** with the direct mechanism, which was unable to pick up on the clear shift of the ESA which occurs rapidly after photoexcitation. It was possible to fit a parallel excimer decay mechanism to the **EH** data, and indeed the lack of distinct spectral features in the broad **EH** ESA makes a definitive model difficult. We acknowledge that the inherently heterogeneous nature of films means that we cannot preclude the possibility that defect sites or sites with less favorable SF intermolecular geometries may be present in certain films, which do not act as an intermediate. The general model presented here, however, fit the data for each TDPP well, and is able to account for the weak excimer-like emission observed by TRF for all derivatives which appears <20 ps and decays with time constants close to those found from the kinetic model in eq 1.

Nanosecond Transient Absorption Spectroscopy of Annealed Films. Nanosecond transient absorption (nsTA) measurements were carried out on film samples excited at 515 nm in order to characterize any long-lived species. Spectra from 50−4000 ns are shown in Figure S5, and the corresponding

kinetic data in Table S3. In all four TDPP molecules, an alternating signal of positive and negative peaks between 500−625 nm is observed, which matches that observed at longer times in the fsTA spectra (see overlay in Figure S13), and persists hundreds of ns to µs. The decay of this species was approximated by a biexponential fit, although triplet−triplet annihilation is a bimolecular process. We attribute the short and long components to short-range triplet−triplet annihilation vs triplets that are able to diffuse away from one another before annihilating. The $T_n \leftarrow T_1$ spectrum strongly overlaps the GSB, which is not uncommon in SF chromophores,[19,29,53] and has been seen in previously published triplet spectra for DPP.[73] Triplet sensitization experiments were next performed on films of the four TDPP derivatives using $PdPc(OBu)_8$ as the triplet sensitizer, as in previous work on DPP.[50] Although to prevent phase segregation the sensitized films were not annealed, the resulting sensitized triplet spectra can be seen in Figure S7. Traces at long delay times in the fsTA spectra for the as-deposited films (Figure S4) can be matched to the sensitized spectra, although differences emerge due to the slightly different ground state absorption of TDPP in the presence of $PdPc(OBu)_8$ (Figure S7). The sensitized spectra also resemble the annealed nsTA spectra, with any differences attributable to the strong overlap of the GSB, which differs between as-deposited and annealed films. Given this and its similarity to the triplets previously observed in DPPs,[72,73] the nsTA signal is assigned to the TDPP triplet state.

Triplet Yield Analysis. When singlet fission is energetically and kinetically favorable, two triplets can be generated per photon absorbed. In order to calculate triplet yields, several methods are commonly employed. One of these methods is triplet sensitization with a suitable chromophore such as $PdPc(OBu)_8$, that can undergo triplet energy transfer to the triplet state of the chromophore of interest, after which an extinction coefficient for the triplet−triplet absorption spectrum can be calculated.[77] The sensitized triplet spectra in Figure S7 are useful for qualitative comparison with the nsTA data, but they differ significantly enough in their GSB spectrum upon annealing (Figure S3) that a calculation of extinction coefficients from the ΔA spectra would be inaccurate. Another method uses known extinction coefficients to construct and scale basis spectra to calculate a yield from global analysis of the fsTA data.[53,78] In addition to the lack of information about relative extinction coefficients in the TDPP films, the presence of the intermediate state makes this method inaccurate for this system. Additionally, we are unable to employ methods used to quantify SF in chromophores such as pentacene, which possess spectrally distinct features for the singlet and triplet states, as the absorption of these states strongly overlap in TDPP.

However, the singlet depletion method described by Carmichael and Hug[77] was successfully adapted for triplet yield determination in several rylene-based SF chromophores and benchmarked using pentacene.[18,19] This method was also used to calculate the triplet yields in PhTDPP and compared favorably to triplet sensitization methods.[50] Although **Me**, **C6**, and **TEG** should be completely converted to triplet states by the end of the fsTA experiment, **EH** has a significant contribution at long delay times from the excimer species. We therefore restrict our yield analysis to nsTA spectra as any excimer species should be absent on this time scale: as the triplet yield for our purposes is most useful as a measure of relative comparison, it is then possible to perform the triplet yield calculation in the same manner for all four derivatives.

To obtain the triplet ESA spectrum, it is assumed that

$$A(T_1) = \Delta A_{50ns} + [\Phi_T \times A(S_0)] \qquad (2)$$

where $A(T_1)$ is triplet−triplet absorption, $A(S_0)$ is the expected GSB for one singlet depleted per triplet, and ΔA_{50ns} is the nsTA spectrum of the film at 50 ns, after which state B should be fully converted into the triplet state. Therefore, the singlet GSB spectrum is added to the nsTA ΔA spectrum until a singlet ground state peak (initially appearing as negative ΔA signal) is removed, and the region of the peak becomes linear in the $A(T_1)$ spectrum. This is based on the assumption that peaks in $A(S_0)$ must be different than peaks in $A(T_1)$; the singlet depletion method is most accurate when the region chosen for analysis has a sharp feature.

To determine the amplitude of $A(S_0)$ to be added, the excitation density of the sample is calculated as detailed in the Supporting Information (eq S1), knowing the thickness, molecular density, and absorbance of the TDPP film, as well as the pump power and spot size. By adding multiples of this spectrum (i.e., $\Phi_T = 10\%-200\%$) to the ΔA nsTA spectrum of each TDPP film at 50 ns, we estimate the triplet yields for all four films and their corresponding triplet−triplet absorption spectra $A(T_1)$, shown in Figure S12. The linearity of each GSB addition multiple was evaluated by integration of the area under each curve; by plotting this area A as a function of GSB addition, the yield can be located at $A = 0$, Figure S11. For **Me** the yield is determined to be 200%. For **C6** and **TEG**, the yield is estimated to be 110%. For **EH**, the yield is 70%. The triplet yield error bars are ±20% and mainly arise from the excitation density calculation, so that the reported yields are most useful for a relative comparison across the series of TDPPs studied. The 200% yield measured for **Me** is the theoretical maximum, irrespective of the error bars. **Me** has the highest yield and corresponding highest SF rate; **C6** and **TEG** have equivalent yields and comparable time constants on the order of several hundreds of ps. Triplet formation in **EH** occurs on a much slower time scale and has the lowest yield.

Singlet Fission Coupling Energies. In order to further investigate the effect of intermolecular geometry on SF, the electronic couplings for singlet fission were calculated using the methodology described by Berkelbach et al. for the super-exchange mechanism:[25]

$$\langle S_1 S_0^{(1)} | \hat{V}_{el} | T_1 T_1^{(1)} \rangle = \langle S_1 S_0^{(0)} | \hat{H}_{el} | T_1 T_1^{(0)} \rangle$$
$$- 2 \frac{V_{S_1 S_0, CA} V_{CA, TT} - V_{S_1 S_0, AC} V_{CA, TT}}{[E(CT) - E(TT)] + [E(CT) - E(S_1)]} \qquad (3)$$

The couplings V_{if} between the singlet excited state, the CT state, and the correlated triplet pair can be determined using one-electron orbital coupling matrix elements $J_{AB} = \langle \varphi_A | \hat{F} | \varphi_B \rangle$ where A and B represent the HOMO or LUMO on different chromophores in the dimer pair, and $\hat{F}$ is the Fock operator. The direct coupling $\langle S_1 S_0 | \hat{H}_{el} | T_1 T_1 \rangle$ is assumed to be small compared to the one-electron couplings, V_{if}. Assuming that $E(TT) \approx E(S_1) = 2.2$ eV, the equation for the one-electron coupling results:

$$V_{1e} \approx \frac{\sqrt{\frac{3}{2}} (J_{HL} J_{LL} - J_{LH} J_{HH})}{E(CT) - E(S_1)} \qquad (4)$$

J_{AB} was calculated using the fragment orbital approach in the Amsterdam density functional (ADF) package (B3LYP/TZ2P).[24] Because extracted monomeric structures from

diffraction can be imprecise,[55] the monomer geometry of **Me**-TDPP was optimized and then placed in a slip-stacked dimer arrangement as determined by each of the four crystal structures (i.e., Δx and Δy values in Table 1). The side chains are not expected to change the coupling values substantially compared to the effect of slip-stacking, and so for each geometry **Me** was used as the side chain for all four calculations.

The value of E_{CT} for each derivative can also be determined, using a Weller-like equation:[79]

$$E_{CT} = IP + EA + E_{solv} + E_{elec} \qquad (5)$$

where IP is the ionization potential, EA is the electron affinity, E_{solv} is the solvation energy for a dimer pair undergoing SF in a crystal, and E_{elec} is the electrostatic energy between the ion pair formed in the CT state. IP and EA were determined using density functional theory to be 6.8 eV and −1.2 eV, respectively. The solvation and electrostatic energies were calculated as in previous SF studies treating the superexchange mechanism[25,52] using the fully classical Direct Reaction Field (DRF) Force Field method.[80] In this method, the known crystal structures of the four derivatives are used to determine the energies of interest by embedding an ion pair in the center of a crystal. For consistency with the coupling calculations, the various side chains were all replaced by **Me**, which causes very little change in the overall CT energy (0.07−0.04 eV).

The resulting one-electron couplings and CT energies are given in Table 3. Both **Me** and **C6** have the strongest coupling

Table 3. One-Electron Orbital Coupling Matrix Elements, CT Energies, and Overall One-Electron Couplings for SF in the Four TDPP Derivatives

TDPP	J_{HH} (meV)	J_{HL} (meV)	J_{LH} (meV)	J_{LL} (meV)	E_{CT} (eV)	V_{1e} (meV)
Me	15.7	−161	176	121	2.81	48.0
C6	159	−60.0	75.8	198	2.91	42.3
TEG	−24.5	38.5	−45.2	−82.7	3.28	5.30
EH	94.3	−7.79	26.9	108	3.01	5.55

energies (40−50 meV) and show fast SF, while **EH** has much weaker coupling (~5 meV) and shows slow SF. While it is not surprising that **Me** shows the strongest coupling (48.0 meV) given that it has the shortest intermolecular distance $r_{\pi-\pi}$ we note that **EH** and **C6** have very similar values of $r_{\pi-\pi}$ yet differ by almost a factor of 10 in their one-electron coupling. As expected, intermolecular geometry plays a large role in determining the SF coupling.

TEG has similarly weak coupling to **EH**, yet does exhibit relatively fast SF in our experiments; we anticipate that the nonalkyl nature of this tail may change the electronic properties or intermolecular interactions of the molecule in a way that is not captured by the present calculation. However, as mentioned above, the rate constant for triplet formation (k_2) in the proposed kinetic model for **TEG** may be difficult to interpret based on global analysis.

■ DISCUSSION

TDPP Singlet Fission Yields and Kinetics. From the transient absorption measurements we observe triplet yields in excess of 100% for all but one of the TDPP derivatives, with triplet formation occurring on the order of tens to hundreds of picoseconds. The trend in triplet yields tracks the SF rates calculated from global analysis of the fsTA data. All four

compounds show evidence of the excimer-like state prior to triplet formation, which is formed rapidly in **Me** (τ_1 = 2.7 ps) and **C6** (τ_1 = 0.9 ps) but somewhat more slowly in **TEG** (τ_1 = 10.1 ps) and **EH** (τ_1 = 16 ps). From the excimer-like state, triplet formation is fast in **Me** (τ_2 = 22 ps) and moderately fast in **C6** (τ_2 = 336 ps) and **TEG** (τ_2 = 195 ps). Yet, for **EH**, triplet formation is not very competitive with the intrinsic excimer state decay to ground state (τ = 2.4 ns). Based on the 70% triplet yield of **EH** and observed τ_2 = 1.6 ns, we calculate that triplet formation takes place in τ_{SF} = 1.2 ns.

Role of the Excimer-Like Intermediate in Singlet Fission. For the observed TDPP intermediate, the broad, red-shifted, weak emission suggests the presence of an excimer in which excitation energy is shared between adjacent chromophores. Its lifetime is relatively short (22 ps−1.2 ns) compared to most excimers,[81,82] most likely because SF within the excimer kinetically outcompetes its natural decay time. The small discrepancy in the excimer lifetimes from TRF and the excimer-to-triplet time constants found from the fsTA is perhaps not surprising, when considering that the measured emission is extremely weak (QY < 1%). It is likely that the TRF kinetics are contaminated by the presence of any defect sites or grain boundaries in the films, slightly obscuring the intrinsic lifetime of the intermediate state.

With crystal structures for the present TDPP derivatives that show intermolecular distances on the order of 3.3−3.7 Å, it is not surprising that these strongly coupled chromophores form excimer states, commonly understood as a superposition of the singlet excited state configurations $^1*M_AM_B$ and $M_A{}^1*M_B$ as well as the intermolecular charge-transfer states $M_A{}^+M_B{}^-$ and $M_B{}^+M_A{}^-$.[82,83] Although excimers have previously been considered trap states for SF,[10,27,82,84] we find here that the presence of this intermediate in TDPP does not preclude high triplet yields (70−200%).

Intermediate states have been observed in a handful of systems undergoing SF. In the case of terrylene, excimer formation was found to precede fast triplet formation.[18] Several experimental studies indicate the presence of an excimer intermediate preceding triplet formation in pentacene,[5] TIPS-pentacene,[24] tetracene,[27] and TIPS-tetracene,[28] which was equated with the multiexciton state, $^1(T_1T_1)$. For a concentrated solution of TIPS-tetracene, the diffusional intermediate has clear excimer-like emission with a lifetime of 8 ns,[28] whereas for a benzene-linked dimer of tetracene, the observed intermediate lifetime is 500 ps, with no excimer emission in solution.[27] In both tetracene studies, $^1(T_1T_1)$ gated SF in solution, with the ESA resembling that of both the singlet and triplet excitons. The nature of $^1(T_1T_1)$ is still uncertain, and has been invoked in the quantum coherent fission mechanism, in which photoexcitation creates an electronic superposition involving $^1(S_1S_0)$, the ME state, and a virtual CT state,[85] or as a distinct intermediate on the way to generating free triplet carriers.[28] However, excimer states can have varying degrees of exciton vs charge resonance, meaning that excimers can have high CT character. Although the intermediate state observed here experimentally does not appear to be a pure CT state, our calculations treat SF with a superexchange mechanism, as the direct mechanism would not include the participation of any intermediate state.

Akin to the intermediate state observed in tetracene, the spectra for this state in **Me**, **C6**, and **TEG** (Figure 6) bear similarity to both the singlet and triplet absorption signatures, which is most notable for **Me** and **TEG**, where the negative

GSB signal shifts to align with the negative peaks in the triplet spectrum. The $^1(T_1T_1)$ energy is commonly taken to be $2E(T_1)$, which for TDPP would be ∼2.2 eV, quite close in energy to S_1. From the excimer fluorescence onset, its energy is ∼2.1 eV. The energetic proximity of this state to the lowest excited singlet state in these derivatives as well as its transient spectra suggests that the excimer-like state may be the multiexciton $^1(T_1T_1)$ state that precedes formation of the uncorrelated triplet excitons. However, determining the exact energy from excimer emission is challenging, due to the possibility that the excited state and ground state minima are offset along some molecular coordinate, leading to emission which reaches the slope of the ground state surface above its minima.[82,86] In such a case, a Franck−Condon progression would be expected, as is observed in the IRF-limited S_1 spectra (Figure 4) in particular for **Me**, **C6**, and **TEG**. This fluorescence signature is peaked at roughly the same energy as the monomer fluorescence (∼560 nm, or 2.2 eV) for all derivatives, suggesting SF from this initial state is roughly isoergic. Despite the low emission energy of the excimer state suggesting that SF is endoergic in DPP, this is not necessarily the case due to unfavorable Franck−Condon factors. The effect of temperature on DPP SF, i.e., whether it is thermally activated, remains to be investigated. It is also possible that the excimer state could be formed from the initial excited state via relaxation along a CT-state energy surface, with increasing CT character in the excited state going from **Me** to **EH**; we next consider how CT configurations may promote SF.

Charge Transfer Stabilization. Although pure excimer states may act as trap states, here the high degree of CT-character in the ground and excited states of DPP can enhance the involvement of the CT configurations in the excimer state. CT states are thought to play an important role in mediating SF in several chromophores, such as pentacene, certain "push-pull" polymers, and diphenylisobenzofuran.[29,87−90] It has also been argued that fast SF requires CT-state participation, either via a singlet excited state with strong CT character, or as a virtual state accessible through superexchange,[26,67] although this may not be essential.[55,91]

An excimer state with significant CT character lies on the continuum between a nonpolar excimer $^1*(MM)$ and a polar CT state (M^+M^-). Given that CT states may facilitate fast SF through superexchange,[23] this may explain why SF appears to be more favorable in **Me**, **C6**, and **TEG**. Indeed, enhancing the CT character has been used as a design principle for SF chromophores,[29,89] and the intermolecular geometries of the single crystal structure dimers in Figure 1 show how intermolecular CT interactions arise in the solid-state packing of TDPP derivatives. In a recent study on a DPP dimer, the interconversion of Frenkel states to excimer states was observed through stabilization by interchromophore donor−acceptor interactions.[49] In addition, modeling the solid-state absorption spectra of DPP required a mixture of CT and Frenkel exciton states[44] to properly describe the Davydov splitting, and the charge-transfer integrals in DPP crystals are known to depend strongly on their slip-stacked arrangement,[39] which maximizes intermolecular donor−acceptor CT interactions in the crystal.[44,57] Our preliminary calculations for the four derivatives show that the intermolecular geometries of **Me** and **C6** result in lower E_{CT} energies and much stronger SF couplings. Indeed, earlier calculations on DPP found that the triplet−triplet absorption possesses high CT character,[70] and that the intermolecular interaction in solids of TDPP lead to admixtures

of CT configurations which stabilize the lowest excited state.[44] Our future theoretical work on DPP will investigate the CT state and the nature of the excimer state, as well as why **C6** shows similarly favorable SF coupling but has a much slower SF rate than **Me**. Here, we have taken ΔG_{SF} to be isoergic for all four derivatives, similar to the approach in Yost et al.[55] for a variety of pentacene and tetracene derivatives with different packing geometries. However, it is possible that the S_1-T_1 splitting would be affected by the amount of CT character in the excited states, or by the degree of planarity in the solid, which may affect the energetics.[92]

The relationship of the ME state to the excimer intermediates observed in the solution-phase studies is relatively unexplored. Recent theoretical work has begun to explicitly treat excimer formation in tetracene dimers; formation of the ME state was more favorable from relaxed excimer geometries.[79] Presumably, different SF chromophores will have varying degrees of Frenkel exciton-CT state mixing within the ME state, such that the ME state may differ spectrally across a series of SF molecules. For the observed intermediate, given that TDPP displays strong CT mixing, precise differentiation in terms between excimer and CT state remains to be determined and likely varies in different packing motifs.

Nevertheless, a qualitative assessment of the importance of the intermolecular D−A arrangement, in which the thiophene ring lies on top of the DPP core, can be made, as supported by the SF coupling calculations. This interaction appears to be enhanced for **Me** and **C6**, which have strong coupling energies; **EH** has much weaker coupling along with packing which reduces this CT interaction in which only the edges of the thiophene ring and DPP core overlap slightly, and the sulfur atoms in thiophene are furthest from the nitrogen atoms of the DPP core. In between the strongly overlapped structure of **Me** and the strongly offset **EH**, **TEG** has rings that straddle the core and rings of the adjacent **TEG** molecules.

Interestingly, **TEG** presents a somewhat different picture: D−A interactions are less pronounced, and the calculated SF coupling is on the order of **EH**. However, the D−A interactions appear more significant than in **EH** in the crystal structure, and most notably, the fluorescence spectra are markedly different from the other TDPP derivatives. The intermediate state ESA and psTRF spectra of **TEG** have relatively narrow peaks and vibronic structure compared to the broad, extremely weak intermediates in **Me** and **C6**. Perhaps the presence of triethylene glycol chains in place of simple alkyl chains enhances the CT character of the **TEG** intermediate. Other interactions involving the oxygen atoms in the long triethylene glycol tails may be important in **TEG** given that similar side chains have been shown to enhance the dielectric constant of various polymers,[93] and the tails in **TEG** pack in such a way that they have some association with neighboring molecules. We attribute the discrepancy between the calculated coupling and the experimental rate to such interactions, which may not be captured in the theoretical model. Here we have considered only the most closely associated dimer pairs, and further work is needed to understand how the electronic structure of **TEG** may differ from that of other TDPP derivatives. However, considering the electronic coupling alone does not account for small changes in the free energy of the SF process from the excimer state that are reflected in the variations in excimer emission wavelengths, so that these free energy changes may

also be responsible for the differences observed between the computed and observed SF rates.

Finally, shorter interchromophore distances and higher degrees of thiophene ring-DPP core coplanarity could also enhance the donor−acceptor unit overlap: **Me** is most planar ($\theta = 2.7°$) and has the smallest π−π distance. The triplet yield for **Me** is 200%, and its SF rate is far faster than rates reported previously for DPP SF. In contrast, the branched side chains of molecule **EH** lead to decreased planarity of the conjugated system and weaker D−A interactions in the crystal structure, which disfavors triplet formation via SF. Indeed, SF is barely competitive with decay of the excimer to ground state in this system, and the triplet yield is less than 100%.

CONCLUSIONS

TDPPs are strongly absorbing, robust SF chromophores, which can be solubilized by 2,5-dialkyl substitution. In this study, four TDPP derivatives were synthesized with different side chain substituents, methyl (**Me**), n-hexyl (**C6**), triethylene glycol (**TEG**), and 2-ethylhexyl (**EH**), that display separate and distinct molecular geometries with varied intermolecular π−π interactions. The SF dynamics in thin films of these molecules were characterized by femtosecond transient absorption (fsTA) and time-resolved fluorescence (TRF) spectroscopies. By comparing structural information from single crystal diffraction and thin film grazing incidence wide-angle X-ray scattering (GIWAXS), the SF rates of each derivative can be related to their thin film morphology, identifying those molecular and packing motifs that enhance SF efficiency. Furthermore, intermediate states are identified prior to triplet state formation, which possess many characteristics of excimer states. Despite the presence of such intermediates, sizable triplet yields of 70−200% are found for films of the present TDPP molecules, indicating that this state does not act as a trap but rather as a precursor to triplet formation. Fast singlet fission is observed in **Me** and **C6**, which both adopt molecular packing that enhances the D−A interaction between the thiophene ring and the DPP core. This arrangement is further enhanced by the small π−π stacking distance in **Me**; this molecule displays the most rapid SF ($\tau_{SF} = 22$ ps) and a 200% triplet yield. We find that the one-electron couplings for these derivatives are on the order of 40−50 meV. The D−A interaction is present to a lesser degree in **TEG**, and here the intermediate state is far more emissive and displays distinct vibronic structure in contrast to the other TDPPs; however, SF takes place in hundreds of ps, similar to **C6**. **EH** does not adopt a packing geometry with strong D−A characteristics, and SF is only slightly competitive with radiative decay from the intermediate. Our calculated one-electron coupling for **EH** is an order of magnitude smaller than **Me** and **C6**. These studies afford a better understanding of parameters that enhance SF in chromophores having strong CT character and provide experimental data for how intermolecular geometry affects SF efficiency. TDPP represents a promising chromophore for future SF-enhanced photovoltaics, given its high stability, synthetic accessibility, and fast SF rate.

ASSOCIATED CONTENT

Ⓢ Supporting Information

The Supporting Information is available free of charge on the ACS Publications website at DOI: 10.1021/jacs.6b05627.

> Additional information on transient absorption analysis and triplet yield analysis (PDF)

X-ray characterization and computational data (CIF)

■ AUTHOR INFORMATION

Corresponding Authors
*g-schatz@northwestern.edu
*t-marks@northwestern.edu
*m-wasielewski@northwestern.edu

Notes
The authors declare no competing financial interest.

■ REFERENCES

(1) Smith, M. B.; Michl, J. *Chem. Rev.* **2010**, *110*, 6891.
(2) Hanna, M. C.; Nozik, A. J. *J. Appl. Phys.* **2006**, *100*, 074510.
(3) Walker, B. J.; Musser, A. J.; Beljonne, D.; Friend, R. H. *Nat. Chem.* **2013**, *5*, 1019.
(4) Musser, A. J.; Liebel, M.; Schnedermann, C.; Wende, T.; Kehoe, T. B.; Rao, A.; Kukura, P. *Nat. Phys.* **2015**, *11*, 352.
(5) Chan, W.-L.; Ligges, M.; Jailaubekov, A.; Kaake, L.; Miaja-Avila, L.; Zhu, X.-Y. *Science* **2011**, *334*, 1541.
(6) Bakulin, A. A.; Morgan, S. E.; Kehoe, T. B.; Wilson, M. W. B.; Chin, A. W.; Zigmantas, D.; Egorova, D.; Rao, A. *Nat. Chem.* **2015**, *8*, 16.
(7) Zimmerman, P. M.; Zhang, Z.; Musgrave, C. B. *Nat. Chem.* **2010**, *2*, 648.
(8) Piland, G. B.; Bardeen, C. J. *J. Phys. Chem. Lett.* **2015**, *6*, 1841.
(9) Burdett, J. J.; Bardeen, C. J. *Acc. Chem. Res.* **2013**, *46*, 1312.
(10) Schrauben, J. N.; Ryerson, J. L.; Michl, J.; Johnson, J. C. *J. Am. Chem. Soc.* **2014**, *136*, 7363.
(11) Ryerson, J. L.; Schrauben, J. N.; Ferguson, A. J.; Sahoo, S. C.; Naumov, P.; Havlas, Z.; Michl, J.; Nozik, A. J.; Johnson, J. C. *J. Phys. Chem. C* **2014**, *118*, 12121.
(12) Wang, C.; Angelella, M.; Kuo, C.-H.; Tauber, M. J. *Proc. SPIE* **2012**, *8459*, 845905.
(13) Wang, C.; Tauber, M. J. *J. Am. Chem. Soc.* **2010**, *132*, 13988.
(14) Varnavski, O.; Abeyasinghe, N.; Arago, J.; Serrano-Perez, J. J.; Orti, E.; Lopez Navarrete, J. T.; Takimiya, K.; Casanova, D.; Casado, J.; Goodson, T. *J. Phys. Chem. Lett.* **2015**, *6*, 1375.
(15) Musser, A. J.; Al-Hashimi, M.; Maiuri, M.; Brida, D.; Heeney, M.; Cerullo, G.; Friend, R. H.; Clark, J. *J. Am. Chem. Soc.* **2013**, *135*, 12747.
(16) Sanders, S. N.; Kumarasamy, E.; Pun, A. B.; Trinh, M. T.; Choi, B.; Xia, J.; Taffet, E. J.; Low, J. Z.; Miller, J. R.; Roy, X.; Zhu, X. Y.;

(17) Ramanan, C.; Smeigh, A. L.; Anthony, J. E.; Marks, T. J.; Wasielewski, M. R. *J. Am. Chem. Soc.* **2012**, *134*, 386.
(18) Eaton, S. W.; Miller, S. A.; Margulies, E. A.; Shoer, L. E.; Schaller, R. D.; Wasielewski, M. R. *J. Phys. Chem. A* **2015**, *119*, 4151.
(19) Eaton, S. W.; Shoer, L. E.; Karlen, S. D.; Dyar, S. M.; Margulies, E. A.; Veldkamp, B. S.; Ramanan, C.; Hartzler, D. A.; Savikhin, S.; Marks, T. J.; Wasielewski, M. R. *J. Am. Chem. Soc.* **2013**, *135*, 14701.
(20) Congreve, D. N.; Lee, J.; Thompson, N. J.; Hontz, E.; Yost, S. R.; Reusswig, P. D.; Bahlke, M. E.; Reineke, S.; Van Voorhis, T.; Baldo, M. A. *Science* **2013**, *340*, 334.
(21) Ehrler, B.; Walker, B. J.; Böhm, M. L.; Wilson, M. W. B.; Vaynzof, Y.; Friend, R. H.; Greenham, N. C. *Nat. Commun.* **2012**, *3*, 1019.
(22) Jadhav, P. J.; Mohanty, A.; Sussman, J.; Lee, J.; Baldo, M. A. *Nano Lett.* **2011**, *11*, 1495.
(23) Greyson, E. C.; Vura-Weis, J.; Michl, J.; Ratner, M. A. *J. Phys. Chem. B* **2010**, *114*, 14168.
(24) te Velde, G.; Bickelhaupt, F. M.; Baerends, E. J.; Fonseca Guerra, C.; van Gisbergen, S. J. A.; Snijders, J. G.; Ziegler, T. *J. Comput. Chem.* **2001**, *22*, 931.
(25) Berkelbach, T. C.; Hybertsen, M. S.; Reichman, D. R. *J. Chem. Phys.* **2013**, *138*, 114103.
(26) Monahan, N.; Zhu, X. Y. *Annu. Rev. Phys. Chem.* **2015**, *66*, 601.
(27) Korovina, N. V.; Das, S.; Nett, Z.; Feng, X.; Joy, J.; Haiges, R.; Krylov, A. I.; Bradforth, S. E.; Thompson, M. E. *J. Am. Chem. Soc.* **2016**, *138*, 617.
(28) Stern, H. L.; Musser, A. J.; Gelinas, S.; Parkinson, P.; Herz, L. M.; Bruzek, M. J.; Anthony, J.; Friend, R. H.; Walker, B. J. *Proc. Natl. Acad. Sci. U. S. A.* **2015**, *112*, 7656.
(29) Busby, E.; Xia, J.; Wu, Q.; Low, J. Z.; Song, R.; Miller, J. R.; Zhu, X. Y.; Campos; Luis, M.; Sfeir, M. Y. *Nat. Mater.* **2015**, *14*, 426.
(30) Chandran, D.; Lee, K.-S. *Macromol. Res.* **2013**, *21*, 272.
(31) Harschneck, T.; Zhou, N.; Manley, E. F.; Lou, S. J.; Yu, X.; Butler, M. R.; Timalsina, A.; Turrisi, R.; Ratner, M. A.; Chen, L. X.; Chang, R. P. H.; Facchetti, A.; Marks, T. J. *Chem. Commun.* **2014**, *50*, 4099.
(32) Karsten, B. P.; Bouwer, R. K. M.; Hummelen, J. C.; Williams, R. M.; Janssen, R. A. J. *Photochem. Photobio. Sci.* **2010**, *9*, 1055.
(33) Loser, S.; Bruns, C. J.; Miyauchi, H.; Ortiz, R. P.; Facchetti, A.; Stupp, S. I.; Marks, T. J. *J. Am. Chem. Soc.* **2011**, *133*, 8142.
(34) Mei, J.; Graham, K. R.; Stalder, R.; Tiwari, S. P.; Cheun, H.; Shim, J.; Yoshio, M.; Nuckolls, C.; Kippelen, B.; Castellano, R. K.; Reynolds, J. R. *Chem. Mater.* **2011**, *23*, 2285.
(35) Li, Y.; Sonar, P.; Murphy, L.; Hong, W. *Energy Environ. Sci.* **2013**, *6*, 1684.
(36) Naik, M. A.; Patil, S. *J. Polym. Sci., Part A: Polym. Chem.* **2013**, *51*, 4241.
(37) Qu, S.; Tian, H. *Chem. Commun.* **2012**, *48*, 3039.
(38) Dhar, J.; Venkatramaiah, N.; Anitha, A.; Patil, S. *J. Mater. Chem. C* **2014**, *2*, 3457.
(39) Calvo-Castro, J.; Warzecha, M.; Kennedy, A. R.; McHugh, C. J.; McLean, A. J. *Cryst. Growth Des.* **2014**, *14*, 4849.
(40) Bürckstümmer, H.; Weissenstein, A.; Bialas, D.; Würthner, F. *J. Org. Chem.* **2011**, *76*, 2426.
(41) Naik, M. A.; Venkatramaiah, N.; Kanimozhi, C.; Patil, S. *J. Phys. Chem. C* **2012**, *116*, 26128.
(42) Adachi, M.; Nakamura, S. *J. Phys. Chem.* **1994**, *98*, 1796.
(43) Dhar, J.; Karothu, D. P.; Patil, S. *Chem. Commun.* **2015**, *51*, 97.
(44) Kirkus, M.; Wang, L.; Mothy, S.; Beljonne, D.; Cornil, J.; Janssen, R. A. J.; Meskers, S. C. J. *J. Phys. Chem. A* **2012**, *116*, 7927.
(45) Langhals, H.; Potrawa, T.; Nöth, H.; Linti, G. *Angew. Chem., Int. Ed. Engl.* **1989**, *28*, 478.
(46) Zhang, X.; Richter, L. J.; DeLongchamp, D. M.; Kline, R. J.; Hammond, M. R.; McCulloch, I.; Heeney, M.; Ashraf, R. S.; Smith, J. N.; Anthopoulos, T. D.; Schroeder, B.; Geerts, Y. H.; Fischer, D. A.; Toney, M. F. *J. Am. Chem. Soc.* **2011**, *133*, 15073.

(47) Iqbal, A.; Jost, M.; Kirchmayr, R.; Pfenninger, J.; Rochat, A.; Wallquist, O. *Bull. Soc. Chim. Belg.* **1988**, *97*, 615.

(48) Stas, S.; Sergeyev, S.; Geerts, Y. *Tetrahedron* **2010**, *66*, 1837.

(49) Kirkus, M.; Janssen, R. A. J.; Meskers, S. C. J. *J. Phys. Chem. A* **2013**, *117*, 4828.

(50) Hartnett, P. E.; Margulies, E. A.; Mauck, C. M.; Miller, S. A.; Wu, Y.; Wu, Y.-L.; Marks, T. J.; Wasielewski, M. R. *J. Phys. Chem. B* **2016**, *120*, 1357.

(51) Renaud, N.; Sherratt, P. A.; Ratner, M. A. *J. Phys. Chem. Lett.* **2013**, *4*, 1065.

(52) Mirjani, F.; Renaud, N.; Gorczak, N.; Grozema, F. C. *J. Phys. Chem. C* **2014**, *118*, 14192.

(53) Roberts, S. T.; McAnally, R. E.; Mastron, J. N.; Webber, D. H.; Whited, M. T.; Brutchey, R. L.; Thompson, M. E.; Bradforth, S. E. *J. Am. Chem. Soc.* **2012**, *134*, 6388.

(54) Dillon, R. J.; Piland, G. B.; Bardeen, C. J. *J. Am. Chem. Soc.* **2013**, *135*, 17278.

(55) Yost, S. R.; Lee, J.; Wilson, M. W. B.; Wu, T.; McMahon, D. P.; Parkhurst, R. R.; Thompson, N. J.; Congreve, D. N.; Rao, A.; Johnson, K.; Sfeir, M. Y.; Bawendi, M. G.; Swager, T. M.; Friend, R. H.; Baldo, M. A.; Van Voorhis, T. *Nat. Chem.* **2014**, *6*, 492.

(56) Arias, D. H.; Ryerson, J. L.; Cook, J. D.; Damrauer, N. H.; Johnson, J. C. *Chemical Science* **2016**, *7*, 1185.

(57) Mizuguchi, J.; Homma, S. *J. Appl. Phys.* **1989**, *66*, 3104.

(58) Soldatova, A. V.; Kim, J.; Rizzoli, C.; Kenney, M. E.; Rodgers, M. A. J.; Rosa, A.; Ricciardi, G. *Inorg. Chem.* **2011**, *50*, 1135.

(59) Jiang, Z. *J. Appl. Crystallogr.* **2015**, *48*, 917.

(60) Hailey, A. K.; Hiszpanski, A. M.; Smilgies, D.-M.; Loo, Y.-L. *J. Appl. Crystallogr.* **2014**, *47*, 2090.

(61) Peng, J.; Guo, X.; Jiang, X.; Zhao, D.; Ma, Y. *Chem. Sci.* **2016**, *7*, 1233.

(62) Singh-Rachford, T. N.; Castellano, F. N. *J. Phys. Chem. A* **2008**, *112*, 3550.

(63) Wu, T. C.; Congreve, D. N.; Baldo, M. A. *Appl. Phys. Lett.* **2015**, *107*, 031103.

(64) Zamis, T. M.; Parkhurst, L. J.; Gallup, G. A. *Comput. Chem.* **1989**, *13*, 165.

(65) Young, R. M.; Singh, A. P. N.; Thazhathveetil, A.; Cho, V. Y.; Zhang, Y.; Renaud, N.; Grozema, F. C.; Beratan, D. N.; Ratner, M. A.; Schatz, G. C.; Berlin, Y. A.; Lewis, F. D.; Wasielewski, M. R. *J. Am. Chem. Soc.* **2015**, *137*, 5113.

(66) Henry, E. R.; Hofrichter, J. In *Methods Enzymol.*; Academic Press: New York, 1992; Vol. *210*, p 129.

(67) Smith, M. B.; Michl, J. *Annu. Rev. Phys. Chem.* **2013**, *64*, 361.

(68) Smilgies, D.-M. *J. Appl. Crystallogr.* **2009**, *42*, 1030.

(69) Lunt, R. R.; Giebink, N. C.; Belak, A. A.; Benziger, J. B.; Forrest, S. R. *J. Appl. Phys.* **2009**, *105*, 053711.

(70) Goswami, S.; Winkel, R. W.; Alarousu, E.; Ghiviriga, I.; Mohammed, O. F.; Schanze, K. S. *J. Phys. Chem. A* **2014**, *118*, 11735.

(71) Ghazvini Zadeh, E. H.; Bondar, M. V.; Mikhailov, I. A.; Belfield, K. D. *J. Phys. Chem. C* **2015**, *119*, 8864.

(72) McCusker, C. E.; Hablot, D.; Ziessel, R.; Castellano, F. N. *Inorg. Chem.* **2012**, *51*, 7957.

(73) McCusker, C. E.; Hablot, D.; Ziessel, R.; Castellano, F. N. *Inorg. Chem.* **2014**, *53*, 12564.

(74) Burdett, J. J.; Gosztola, D.; Bardeen, C. J. *J. Chem. Phys.* **2011**, *135*, 214508.

(75) Rao, A.; Wilson, M. W. B.; Albert-Seifried, S.; Di Pietro, R.; Friend, R. H. *Phys. Rev. B: Condens. Matter Mater. Phys.* **2011**, *84*, 195411.

(76) Chung, K.; Kwon, M. S.; Leung, B. M.; Wong-Foy, A. G.; Kim, M. S.; Kim, J.; Takayama, S.; Gierschner, J.; Matzger, A. J.; Kim, J. *ACS Cent. Sci.* **2015**, *1*, 94.

(77) Carmichael, I.; Hug, G. L. *J. Phys. Chem. Ref. Data* **1986**, *15*, 1.

(78) Margulies, E. A.; Wu, Y.-L.; Gawel, P.; Miller, S. A.; Shoer, L. E.; Schaller, R. D.; Diederich, F.; Wasielewski, M. R. *Angew. Chem., Int. Ed.* **2015**, *54*, 8679.

(79) Oevering, H.; Paddon-Row, M. N.; Heppener, M.; Oliver, A. M.; Cotsaris, E.; Verhoeven, J. W.; Hush, N. S. *J. Am. Chem. Soc.* **1987**, *109*, 3258.

(80) Swart, M.; van Duijnen, P. T. *Mol. Simul.* **2006**, *32*, 471.

(81) Margulies, E. A.; Shoer, L. E.; Eaton, S. W.; Wasielewski, M. R. *Phys. Chem. Chem. Phys.* **2014**, *16*, 23735.

(82) Brown, K. E.; Salamant, W. A.; Shoer, L. E.; Young, R. M.; Wasielewski, M. R. *J. Phys. Chem. Lett.* **2014**, *5*, 2588.

(83) Katoh, R.; Katoh, E.; Nakashima, N.; Yuuki, M.; Kotani, M. *J. Phys. Chem. A* **1997**, *101*, 7725.

(84) Liu, H.; Nichols, V. M.; Shen, L.; Jahansouz, S.; Chen, Y.; Hanson, K. M.; Bardeen, C. J.; Li, X. *Phys. Chem. Chem. Phys.* **2015**, *17*, 6523.

(85) Chan, W.-L.; Ligges, M.; Zhu, X. Y. *Nat. Chem.* **2012**, *4*, 840.

(86) Fink, R. F.; Seibt, J.; Engel, V.; Renz, M.; Kaupp, M.; Lochbrunner, S.; Zhao, H.-M.; Pfister, J.; Würthner, F.; Engels, B. *J. Am. Chem. Soc.* **2008**, *130*, 12858.

(87) Yamagata, H.; Norton, J.; Hontz, E.; Olivier, Y.; Beljonne, D.; Brédas, J. L.; Silbey, R. J.; Spano, F. C. *J. Chem. Phys.* **2011**, *134*, 204703.

(88) Johnson, J. C.; Nozik, A. J.; Michl, J. *Acc. Chem. Res.* **2013**, *46*, 1290.

(89) Busby, E.; Xia, J.; Low, J. Z.; Wu, Q.; Hoy, J.; Campos, L. M.; Sfeir, M. Y. *J. Phys. Chem. B* **2015**, *119*, 7644.

(90) Beljonne, D.; Yamagata, H.; Brédas, J. L.; Spano, F. C.; Olivier, Y. *Phys. Rev. Lett.* **2013**, *110*, 226402.

(91) Wang, L.; Olivier, Y.; Prezhdo, O. V.; Beljonne, D. *J. Phys. Chem. Lett.* **2014**, *5*, 3345.

(92) Köhler, A.; Beljonne, D. *Adv. Funct. Mater.* **2004**, *14*, 11.

(93) Donaghey, J. E.; Armin, A.; Burn, P. L.; Meredith, P. *Chem. Commun.* **2015**, *51*, 14115.